

Oxygen-diffusion limited metal combustions in Zr, Ti, and Fe foils: Time- and angle-resolved x-ray diffraction studies

Haoyan Wei,¹ Choong-Shik Yoo,^{1,a)} Jing-Yin Chen,^{1,b)} and Guoyin Shen²

¹Department of Chemistry and Institute for Shock Physics, Washington State University, Pullman, Washington 99164-2816, USA

²HPCAT Geophysical Laboratory, Carnegie Institution of Washington, Argonne, Illinois 60439, USA

(Received 3 January 2012; accepted 24 February 2012; published online 29 March 2012)

The transient phase and chemical transformations of diffusion controlled metal combustions in bulk Zr, Ti, and Fe foils have been investigated, *in situ*, using novel time- and angle-resolved x-ray diffraction (TARXD). The TARXD employs monochromatic synchrotron x-rays and a fast-rotating diffracted beam chopper resolving the diffraction image temporally in time-resolution of $\sim 45 \mu\text{s}$ along the azimuth on a 2D pixel array detector. The metal foil strips ($10\text{--}25 \mu\text{m}$ in thickness) are ignited using a pulsed electrical heating with a typical heating rate of $\sim 10^6 \text{ K/s}$. The x-ray results indicate that the combustion occurs in molten metals, producing a wide range of stoichiometric solid oxides. It reflects an enhanced oxygen solubility and mobility of molten metals with respect to those of solid metals. However, the initial oxides formed are mainly oxygen-deficient metal oxides of ZrO , TiO , and $\text{FeO/Fe}_3\text{O}_4$ — the lowest suboxides stable at these high temperatures. These transition metal monoxides further react with unreacted molten metals, yielding the secondary products of Zr_3O , Ti_3O , and Ti_2O — but not in $\text{FeO/Fe}_3\text{O}_4$. On the other hand, the higher stoichiometric oxides of ZrO_2 and TiO_2 are formed in the later time only on the metal surface. These results clearly indicate that the combustion process of metal strips is diffusion limited and strongly depends on the solubility and diffusivity of oxygen into molten metals. The time-resolved diffraction data reveals no evidence for metal oxidation in solids, but a series of temperature-induced polymorphic phase transitions. The dynamic thermal expansibility of Fe measured in the present fast heating experiments is similar to those in static conditions ($3.3 \times 10^{-5} \text{ /K}$ vs $3.5 \times 10^{-5} \text{ /K}$ for $\alpha\text{-Fe}$ and $6.5 \times 10^{-5} \text{ /K}$ versus $7.0 \times 10^{-5} \text{ /K}$ for $\gamma\text{-Fe}$). © 2012 American Institute of Physics. [<http://dx.doi.org/10.1063/1.3698318>]

I. INTRODUCTION

Transition metals with high oxygen affinities such as Zr, Ti, and Fe can rapidly react with oxygen at high temperatures, yielding a wide range of transition metal oxides. These highly exothermic, self-fueling metal oxidation reactions (or metal combustions) are complex and strongly depend on microstructures, crystal structures, melting temperatures, and oxygen diffusivities of metals and metal oxides. The presence of solid-solid or solid-liquid phase transitions, for example, has a dramatic effect on the ignition process and combustion kinetics, which can lead to a micro-explosion or an interesting “spear point” formation of oxide products.¹ Yet, a wide range of oxidation states viable in these transition metals can give rise to an array of different oxides depending on temperatures and oxygen concentrations and, thereby, greatly complicate the reaction pathways. Furthermore, the dynamic (or transient) nature of combustions may result in the path-dependent phase and chemical changes and quench metastable structures and secondary products. Therefore, obtaining time-resolved structural data during metal

ignitions and combustions are critical to understanding the chemical mechanisms, energetics, and kinetics.

The most critical process governing metal combustions in air is oxygen diffusion, which strongly depends on the microstructure of metal surface. The presence of thin oxide layers on the surface of small metal particles limits the diffusion of oxygen molecules and thus the combustion in solid metals. As a result, the combustion occurs typically from molten phases of metals above the melting temperatures.^{2,3} In contrast, small oxygen-free metal particles (sub- to a few μm in diameter) freshly produced from metallic glass and lamellae metal alloys with nm-scale microstructures can ignite at relatively low temperatures (well below the melting temperatures of metals) and burn nearly completely within very short reaction time ($< 1 \text{ ms}$) to produce highly oxidized products.⁴ Because of large oxygen diffusion barrier of metal oxides and high thermal conductivity of metals, the oxidation reactions of larger metal particles (say $10\text{--}100 \mu\text{m}$) in surrounding air are typically limited to a very thin layer (less than a few μm) — forming huge gas diffusion and reaction barriers and, thus, leaving a significant portion of large fragments unreacted. The delicate balance among thermal (heat) conduction, oxygen (mass) diffusion, and micro (surface) structures is central to controlling chemical mechanisms, energetics, and dynamics of metal combustions. This again

^{a)}Author to whom correspondence should be addressed. Electronic mail: csyoo@wsu.edu. Tel.: (509) 335 – 2712.

^{b)}Present address: Lawrence Livermore National Laboratory, Livermore, CA 94551.

underscores the significance of time-resolved thermal and structural information over the relevant time (1 μ s to 1 ms) and spatial (atomistic) scales.

The present phase and chemical analysis of metal combustions are primarily based on the temperature profile, phase diagram and postburn microprobe composition analysis^{5,6} — not on the real-time structural information. This is unfortunate considering the fact that synchrotron x-ray diffraction is capable of probing structural changes in exothermic solid/solid reactions including self-propagating high-temperature reactions,^{7–9} intermetallic reactions of multilayer nanofolds,^{10,11} and metathesis reactions.^{12,13} It is presumably due to a substantially faster time resolution (in μ s) required for probing metal/gas reactions. Recently, we have developed a relatively simple *in situ* time- and angle-resolved x-ray diffraction (TARXD) technique to measure the structural and chemical evolutions associated with rapidly propagating intermetallic reactions in a μ s time-resolution.¹⁴ In this study, we have applied this TARXD along with the fast time-resolved temperature measurements, probing real-time structural and chemical evolutions associated with oxygen-diffusion limited metal combustions in bulk metallic foils of Zr, Ti, and Fe.

II. EXPERIMENTAL METHODS

Metal foils (99.8% or better purity) of Zr and Ti (25 μ m in thickness from Alfa Aesar) and Fe (10 μ m from Goodfellow) were used for the samples. These metal foils were cut into strips of about 0.15 mm wide and 2–3 mm long for combustion and time-resolved x-ray diffraction experiments (as shown in Fig. 1). The metal strip sample was placed on a nonconductive ceramic substrate and anchored down with copper electrodes at the both ends. The spacing between the two electrodes was about 0.3–0.5 mm. Along with the metal strip thickness and

width, it defines an active combustion volume of about 0.5–2.0 times 10^{-3} mm³. The electrical resistance of metal strips was in the range of 0.2–0.4 Ω measured with a digital multimeter. Underneath the metal strip, a small through-hole of 0.2 mm in diameter was drilled for the incoming x-ray beam. A DC current source (with a 5 A/6 V capacity) was connected to the copper electrodes. The circuit opening and closure were achieved with an electrical relay switch. The electrical pulse from the digital delay generator (SRS DG645) was used as a gate control signal to trigger the electrical relay and initiate metal combustion. Upon pulsed electrical heating, the metal strip quickly reacts with oxygen in air resulting in highly exothermic reactions, emitting intense thermal radiations. The representative snapshot of Zr combustion recorded on a high-speed camera (Photron FastCam SA.1) is shown on the lower left in Fig. 1. A digital phosphor oscilloscope (Tektronix DPO2000 with 100–200 MHz bandwidth) was used to monitor the voltage evolution of the reacting sample.

We used a 6-channel optical pyrometer to measure the temperature evolution of metal strip in combustion, based on the Planck's law.^{15,16} The optical pyrometer was constructed, for each channel, using a photomultiplier tube (Hamamatsu H7732P-11 PMT with a rise time of 2.2 ns), a narrow spectral band-pass filter ($\Delta\lambda = 10$ nm at FWHM in the range of 550–800 nm with an increment of 50 nm), and a set of neutral density (ND) filters to adjust the incident light intensity within the linear response of PMTs. The incident light was transmitted through six optical fibers (each 0.2 mm core diameter) bundled in a hexagonal pattern at the probe side. The PMT signal was recorded onto two oscilloscopes (Tektronix DPO2000) with 50 Ω terminations, matching the cable impedance and thereby avoiding signal distortions from reflections. Before measurements, the entire pyrometer system, including PMTs, fibers, filters and other optics used, was calibrated with a black-body radiation source (BBRS, OL 480 from Optronic Laboratories). Time-resolved temperatures were obtained by fitting the measured emission intensities at six discrete wavelengths to a gray body radiation equation. The uncertainty of dynamic temperatures measured by the present optical pyrometer varies in the range of 3–8%, primarily centered around 5%.

X-ray diffraction experiments were performed using intense monochromatic ($\lambda = 0.8638$ Å) x-rays from the 16IDD/HPCAT beamline at the Advanced Photon Source (APS). A 2D pixel array detector (PILATUS 100 K) was used to record the TARXD image, which had an active area of 83.8×33.5 mm² with 487×195 pixels (each pixel size of 172×172 μ m²). A fast-rotating metal disk (150 mm in diameter) with four orthogonal opening slots of 1.56 degrees was used to chop the diffraction beam into different time domains. In this configuration, a quarter of the chopper disk covers the entire detector area. The chopper was placed in front of the detector with a few millimeters spacing. The incident beam was aligned to the center of the chopper disk along the vertical center of the detector. As the disk rotates, the slot sweeps across the entire detector active area clockwise along the Debye-Scherrer's rings. As a result, small portions of diffraction rings are recorded at different azimuth angles on the detector at different time. Thus, the diffraction beam is dispersed as a function of time, recording the

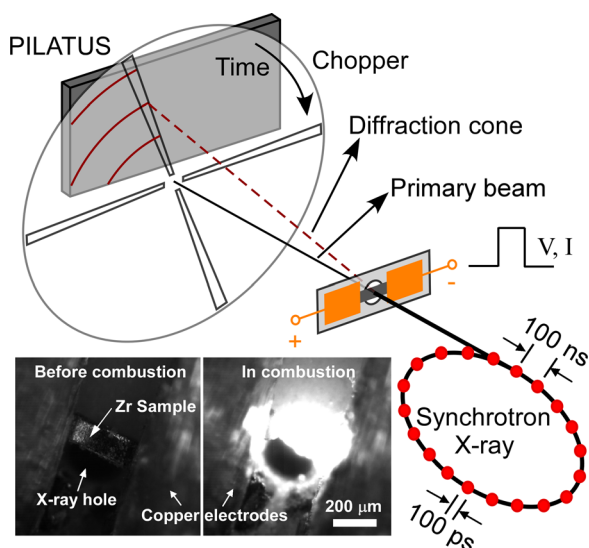


FIG. 1. The experimental setup of time-resolved synchrotron x-ray diffraction to probe the structural and chemical changes of thin metal foils in combustion reaction initiated by electrical pulse heating. The setup utilizes an intense monochromatic x-rays from the APS, a 2D pixel array x-ray detector (PILATUS), and a custom-designed fast-rotating chopper. The lower left images depict the microscopic views of the Zr sample configuration (left) and during combustion (right).

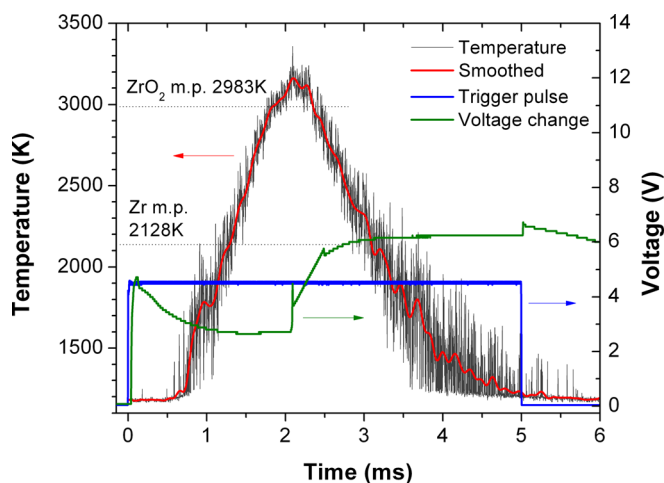


FIG. 2. Time-resolved temperatures of Zr foil in combustion initiated by an electrical pulse heating, plotted together with the trigger pulse (in blue) and the voltage change (green) of the sample. For comparison, the melting temperatures of Zr and ZrO_2 are indicated by horizontal dashed lines.

structural evolution of reacting samples. As the diffraction arcs are recorded continuously, there is no down (or blackout) time in the entire 2D TARXD image representing about 3 ms long event – the critical initial stage in combustions. The time-resolution is then determined by the chopper speed and the slot width. We used a time-resolution of $\sim 45 \mu\text{s}$ in this work. Utilizing the kinetic mode of the detector, multiple frames can be recorded over several hundreds of ms with a relatively small readout time of 3 ms between the frames. This extended record time is important to probe the slow chemical and structural changes occurring later times in metal combustions. More detailed description of the time-resolved x-ray diffraction can be found elsewhere.^{14,17}

III. RESULTS

A. Zirconium combustion

Figure 2 illustrates the measured (in black) and smoothed (red) time-resolved temperatures, as well as voltage (green)

changes of Zr foil during an electric pulse heating (blue). Because of the limited spectral response of PMTs in the range of 185–850 nm, the lower temperature cut-off of the present pyrometer is ~ 1100 – 1200 K. Based on the rising slope of the measured time-resolved temperatures, Zr metal combusts at the heating rate of $\sim 1.5 \times 10^6$ K/s. Extrapolating the heating rate to ambient temperature yields an induction time of less than 0.1 ms. The combustion temperature reaches the maximum at ~ 3200 K (defined as the burst temperature or T_B), which is consistent with the literature values.^{18–20} This burst temperature is higher than the melting temperatures of both Zr (2128 K) and ZrO_2 (2983 K) indicated by dashed lines in Fig. 2.

Figure 3 shows several TARXD images recorded at a time-resolution of $\sim 45 \mu\text{s}$, each representing 3 ms-long structural and chemical changes of a Zr foil during the combustion process. Time runs clockwise. There is a 3 ms blackout time between the images. The onset of the electrical pulse heating is marked by “ t_0 ” with a straight line in Fig. 3(b). The polymorphous transition from hcp α -Zr to bcc β -Zr is also marked with another straight line on the right. A small segment of a white stripe along the radial direction of azimuth in Figs. 3(b)–3(e) represents the doubly exposed area of the diffraction signal from the next incoming slot of the chopper wheel, which is used to locate the onset time in the images.

Figure 4 shows the “caked” TARXD images of Fig. 3, plotting the Bragg 2θ angle in the x-axis as a function of the azimuth angle (time) in the y-axis. The caking process is performed using the Fit2D software.²¹ Similarly, the onset of the heating and the polymorphous transition of Zr are marked by two straight lines in Fig. 4(b). The diffraction lines are also indexed with short color bars on the top of each image. By integrating the caked diffraction patterns for an arbitrary time period (Δt), we then obtain time-resolved diffraction patterns of Zr combustion as shown in Fig. 5. The crystal structures and lattice parameters (both measurements and literature) of relevant Zr polymorphs and its oxides are summarized in Table I.

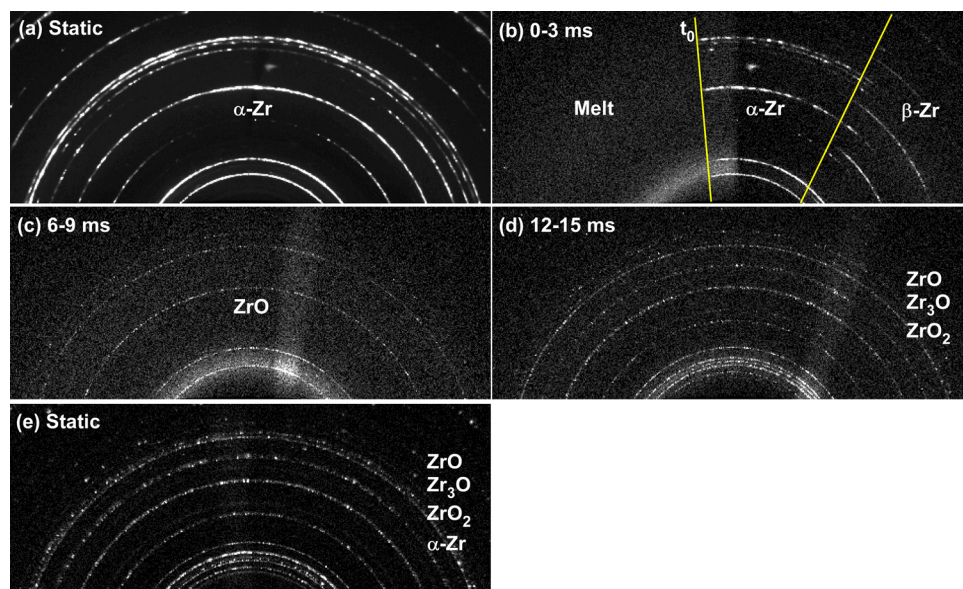


FIG. 3. Static (a), (e) and dynamic (b)–(d) powder x-ray diffraction probing the phase and chemical changes during Zr combustion in air. These TARXD images were obtained with time-resolution of $45 \mu\text{s}$ for each 3 ms long combustion periods. The yellow straight lines in (b) signify the onset of the pulsed heating (t_0) and the α -to- β Zr phase transition. The various oxides formed at different stages of combustion are indicated in (c)–(e).

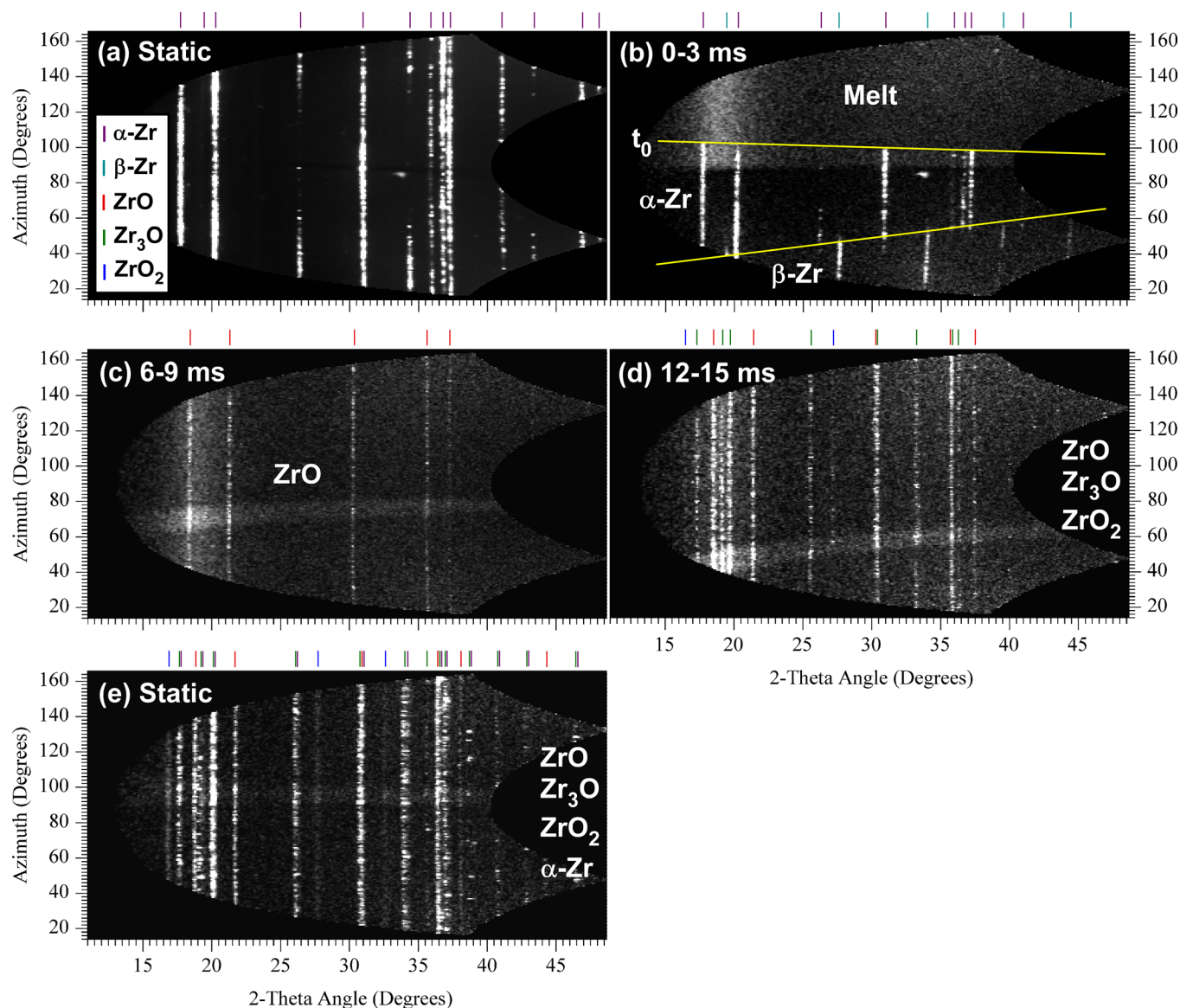


FIG. 4. The caked TARXD images of Fig. 3, as plotted in the Bragg angle 2θ in the x-axis vs azimuth (or time) in the y-axis. The diffraction lines are marked by short color bars at the top to characterize various phases. Also, see Fig. 5 for indexing.

The static pattern on the top in Fig. 5 represents the original Zr in α phase (hcp) with the lattice parameters of $a = 3.241 \text{ \AA}$ and $c = 5.139 \text{ \AA}$. At $\sim 0.8\text{--}0.9 \text{ ms}$ after the ignition, a new set of sharp diffraction lines (indicated by dark cyan) appears indicating the polymorphous transition of α -Zr into bcc β -Zr. Figure 2 also confirms that the corresponding temperature ($\sim 1500\text{--}1700 \text{ K}$) is above the phase transformation point (1136 K). The calculated lattice parameter of β -Zr is $a = 3.620 \text{ \AA}$. This phase transition occurs within about $100\text{--}200 \mu\text{s}$, evidenced by co-existence of the two Zr phases in Figs. 3(b) and 4(b). Subsequently, β -Zr melts as the temperature increases above the melting point, apparent from the broad halo features in the measured x-ray diffraction patterns of Figs. 3(b) and 3(c), 4(b) and 4(c) and 5 (the records from 2.5 to 15 ms). As the temperature decreases after the peak point, high-temperature ZrO in fcc with $a = 4.682 \text{ \AA}$ emerges as the first oxide product at about 6–9 ms, clearly from molten Zr (not solid). As the temperature continually decreases, additional diffraction features appear at $\sim 12\text{--}15 \text{ ms}$, from

two other forms of Zr oxides, cubic ZrO_2 and trigonal Zr_3O . Based on the exponential dependence of temperature on time, the temperature at 12–15 ms is estimated to be around $600\text{--}500 \text{ K}$. Although the measured temperature decreases well below the Zr melting temperature of 2128 K , the halo feature at 6–9 and 12–15 ms is still apparent with the intensity continually decreasing with time. Its presence can be understood in terms of a large temperature gradient in the foil along the x-ray propagation direction. Therefore, the temperature inside the foil can be substantially higher than the surface temperature that the optical pyrometer measures. At substantially later time when the reaction reaches the final state, residual Zr metals in α phase are also observed, in addition to the three Zr oxides mentioned above. The absence of high temperature intermediate phase β -Zr during cooling is likely due to its short transition time, which might have occurred during the readout time. The measured lattice parameters are $a = 5.107 \text{ \AA}$ for fcc ZrO_2 and $a = 5.639 \text{ \AA}$ and $c = 31.407 \text{ \AA}$ for trigonal Zr_3O , in

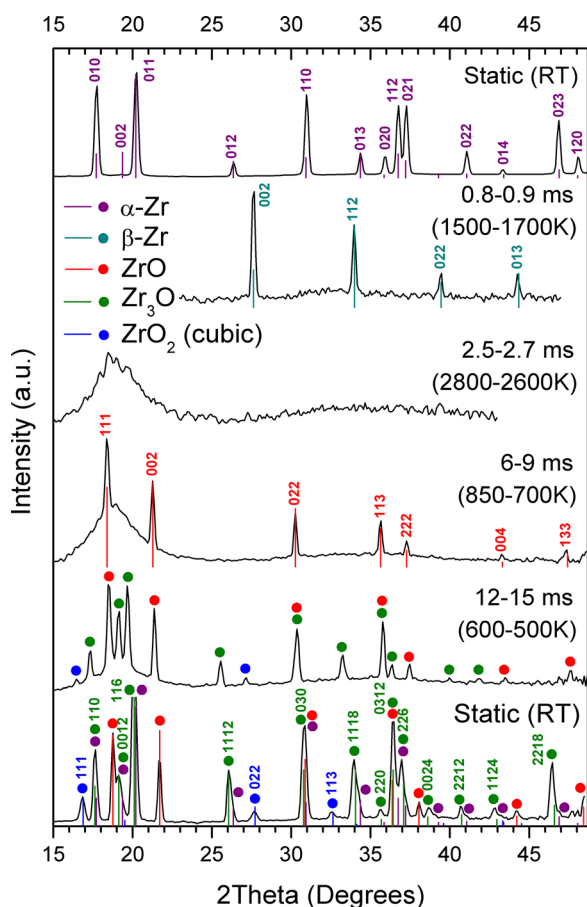


FIG. 5. Time-resolved powder x-ray diffraction patterns of Zr metals in combustion, obtained by integration of the caked TARXD images in Fig. 4 over a discrete time period noted in the figure. The simulated diffraction peaks are superimposed as marked by vertical color lines. The indices of each phase are also indicated.

good accordance with those reported in the literature (see Table I).

Figure 6 shows a full-pattern Rietveld refinement (solid red line) of the measured x-ray diffraction (dotted x) of final combustion products, which yields the detailed chemical composition as summarized in Table I. It shows that ZrO is the primary product at 39.4% of all three Zr oxides. A sizable amount of α -Zr metals ($\sim 33.7\%$) is also present, indicating an incomplete combustion of Zr foil.

B. Titanium combustion

Time-resolved temperatures measured during the combustion of Ti foil are shown in Fig. 7. The measured combustion rate is about 2.8×10^6 K/s, on the same order as that of Zr foil. The burst temperature is around 2620 K, well above the melting points of Ti (1941 K) and rutile-TiO₂ (2113 K). At the moment of sample melting (around 1 ms), a sudden voltage jump to the open circuit state (6 V) is observed as shown by the green line in Fig. 7. This is caused by the fracture of the molten strip sample, also confirmed by the high-speed camera images (the data not shown). The fracture is reproducible for the combustion of Ti and Fe foils (see also Sec. III C). This is unlike the voltage increase in Zr combustion (see the record in Fig. 2 at ~ 2 ms), which does not exhibit a

direct link to Zr and ZrO₂ melting points. The high-speed camera images and post-combustion characterizations, for example, indicate that Zr sample strips have undergone the melting transition and severe mechanical deformation during combustion. Nevertheless, the Zr and oxides strip remains intact even at much higher temperatures than their melting temperatures.

Figure 8 illustrates time-resolved diffraction patterns of the measured TARXD image of Ti foil during combustion. The observed polymorphic phase transitions and the oxidation of molten Ti are analogous to those of Zr in combustion. During the heating stage, hcp α -Ti ($a = 2.953$ Å, $c = 4.665$ Å) transforms into bcc β -Ti ($a = 3.316$ Å) at ~ 1155 K well below the melting temperature of Ti (1941 K). The combustion is initiated from molten Ti, yielding initially cubic γ -TiO (fcc, $a = 4.209$ Å) at about 12–15 ms, then, Ti₂O (trigonal, $a = 2.9745$ Å, $c = 4.7305$ Å) and Ti₃O phases (trigonal, $a = 5.1375$ Å, $c = 9.5524$ Å) at about 36–39 ms. Based on the exponential temperature dependence on time, the temperature is estimated to be 600–500 K. At substantially later time, rutile-TiO₂ (tetragonal, $a = 4.5888$ Å, $c = 2.9558$ Å) also forms in a small amount of $\sim 7\%$ (Table II). The final products after combustion are a mixture of the aforementioned four oxides. Similar to Zr combustion, γ -TiO is the dominant oxide ($\sim 58\%$); however, different from Zr combustion, no residual metallic Ti is observed. Again, the measured lattice parameters of all phases are in good agreement with the values reported in the literature, as compared in Table II.

C. Iron combustion

Figure 9 shows the time-resolved temperature evolution of Fe foil during combustion. The heating rate is about 2.0×10^6 K/s, on the same order observed in Zr and Ti combustions. The burst temperature is about 1870 K as manifested by the spike occurring at about 0.97 ms on the dark gray line in the figure. Based on the analysis of Planck's law fitting (The standard error is about 8%), it is believed that this narrow spike is not noise or bad data but represents an actual temperature. As shown in the left plot in Fig. 9, this temperature is right beyond the melting points of metals Fe (1811 K) and FeO (1650 K), near that of Fe₃O₄ (1870 K). The fracture of molten Fe strip is also confirmed by the concurrent high-speed camera images (not shown). As in the Ti combustion, the melt induced Fe fracture is further indicated by the observed voltage jump across the sample at the same time stamp (green line in Fig. 9).

Figure 10 depicts the time-resolved x-ray diffraction obtained from the measured TARXD images of Fe foils in combustion. During the initial heating stage, two phase transitions occur from α -Fe (bcc) to γ -Fe (fcc) at 1185 K and then to δ -Fe (bcc) at 1667 K. The measured lattice parameters are respectively, 2.868, 3.679, and 2.934 Å for α -, γ -, and δ -Fe, as summarized in Table III. Although we did not observe an independent broad melt feature as in Zr and Ti combustion from x-ray diffraction, a halo background centered around the (011) diffraction of δ -Fe at 1.8–2.1 ms is still clearly present, indicating that Fe has melted. This is

TABLE I. Crystal structures and lattice parameters of Zr and its oxides formed in combustion.

Phase	Content (at. %)	Lattice system	Space group	Lattice parameters (Å)		PDF#
				This work	Literature	
α -Zr (Static)	33.7	Hexagonal	$P6_3/mmc$	$a = 3.241$ $b = 3.241$ $c = 5.139$	$a = 3.232$ $b = 3.232$ $c = 5.147$	05-0665 Ref. 37
β -Zr (0.8–0.9 ms)	–	Cubic	$Im-3m$	$a = 3.620$ $b = 3.620$ $c = 3.620$	$a = 3.620$ $b = 3.620$ $c = 3.620$	Ref. 37
ZrO (6–9 ms)	39.4	Cubic	$Fm-3m$	$a = 4.682$ $b = 4.682$ $c = 4.682$	$a = 4.620$ $b = 4.620$ $c = 4.620$	20-0684 Ref. 37
Zr ₃ O (Final)	19.6	Trigonal	$R32$	$a = 5.639$ $b = 5.639$ $c = 31.407$	$a = 5.563$ $b = 5.563$ $c = 31.185$	74-1272
ZrO ₂ (Final)	7.3	Cubic	$Fm-3m$	$a = 5.107$ $b = 5.107$ $c = 5.107$	$a = 5.129$ $b = 5.129$ $c = 5.129$	81-1550

because Fe stays above the melting temperature only for a short period of time ($\sim 6 \mu s$, as indicated by the width of the narrow spike in Fig. 9). The combustion occurs from molten Fe to produce FeO and Fe₃O₄ at 6–9 ms (or even earlier), corresponding to the temperature of 1650–1550 K near the melting temperatures of Fe (1800 K) and FeO (1650 K) (see Fig. 9). During the cooling period at 24–27 ms (or 1200–1150 K), unreacted Fe changes from high temperature γ phase back to ambient α phase. Both FeO and Fe₃O₄ have cubic structures with lattice parameters $a = 4.286 \text{ Å}$ and $a = 8.391 \text{ Å}$, respectively (Table III). Unlike Ti combustion, large amount of residual metallic Fe (87%) is observed, indicating the partial oxidation. This result confirms that the combustion occurs from molten Fe, which stays only for a short period as aforementioned (Fig. 9). The relatively low combustion temperature of iron ($T_B = 1870 \text{ K}$, for example) with respect to those of Zr (3200 K) and Ti (2600 K) is consistent with the relatively low heat of combustion of iron (FeO, $\Delta H_f^0 = -272.0 \text{ kJ/mol}$) with respect to those of Zr (ZrO₂, -1100.6 kJ/mol) and Ti (TiO, -519.7 kJ/mol).²²

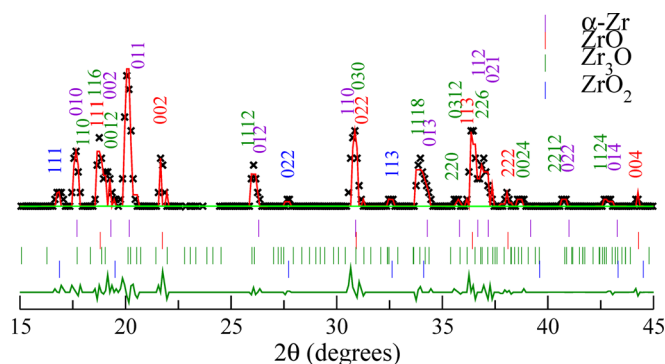


FIG. 6. A full-profile Rietveld refinement (in red) of the measured x-ray diffraction pattern (in x symbols) from Zr combustion products, plotted together with the difference spectrum (in green). The colored tick marks indicate the reflections of Zr and its oxides, as noted at the top of the figure.

IV. DISCUSSION

A. Oxygen diffusion limited primary combustions of metal strips

The time-resolved x-ray diffraction data in Figs. 5, 8, and 10 clearly indicate the oxygen-diffusion limited combustion processes of metal strips. This conclusion stems from (i) combustion initiates only from molten metals. This is likely due to higher solubility of oxygen in molten metals and higher activation barrier for oxygen diffusion through solids. (ii) The primary combustion products are transition metal monoxides, rather than more thermodynamically favored metal dioxides at high pressures and temperatures. Only a small amount of metal dioxides are observed on the surface at the later stage of the reaction. This indicates that the mechanism of metal combustion is kinetically controlled

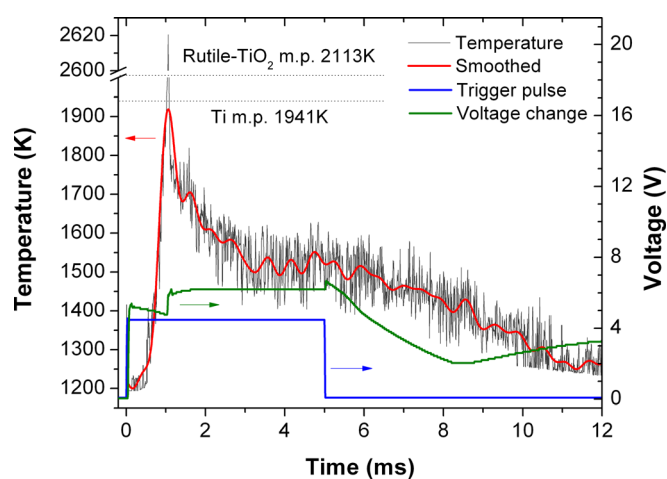


FIG. 7. The temperature evolution of Ti foil in combustion initiated by electrical pulse heating. The trigger pulse and the voltage change on the sample are plotted in blue and green, respectively. The melting points of Ti and TiO₂ (rutile) are indicated by dashed horizontal lines. A sudden voltage jump is observed at the moment when the temperature exceeds Ti melting point and the sample becomes fractured.

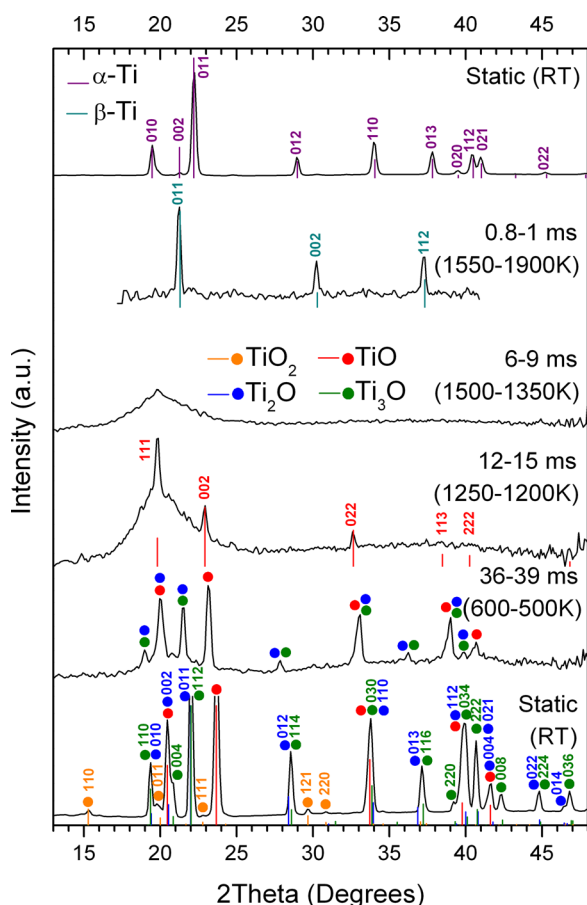


FIG. 8. Time-resolved powder x-ray diffraction patterns of Ti foil in combustion in air. The simulated diffraction peaks are superimposed as marked by vertical color lines. The indices of each phase are also indicated.

largely by oxygen diffusion. (iii) The combustion products at interior in the later time exhibit even lower suboxides such as Zr_3O and Ti_3O/Ti_2O , indicating even a smaller degree of oxygen diffusion in this cooling period.

TABLE II. Crystal structures and lattice parameters of Ti and its oxides formed in combustion.

Phase	Content (at. %)	Lattice system	Space group	Lattice parameters (Å)		PDF#
				This work	Literature	
α -Ti (Static)	—	Hexagonal	$P6_3/mmc$	$a = 2.953$ $b = 2.953$ $c = 4.665$	$a = 2.950$ $b = 2.950$ $c = 4.686$	Ref. 37
β -Ti (0.8–1 ms)	—	Cubic	$Im-3m$	$a = 3.316$ $b = 3.316$ $c = 3.316$	$a = 3.3065$ $b = 3.3065$ $c = 3.3065$	
γ -TiO (Final)	58	Cubic	$Fm-3m$	$a = 4.209$ $b = 4.209$ $c = 4.209$	$a = 4.177$ $b = 4.177$ $c = 4.177$	
Ti_3O (Final)	7.6	Trigonal	$P-31c$	$a = 5.1375$ $b = 5.1375$ $c = 9.5524$	$a = 5.1411$ $b = 5.1411$ $c = 9.5334$	73-1583
Ti_2O (Final)	27.2	Trigonal	$P-3ml$	$a = 2.9745$ $b = 2.9745$ $c = 4.7305$	$a = 2.9593$ $b = 2.9593$ $c = 4.8454$	
TiO_2 -Rutile (Final)	7.2	Tetragonal	$P4_2/mnm$	$a = 4.5888$ $b = 4.5888$ $c = 2.9558$	$a = 4.5937$ $b = 4.5937$ $c = 2.9581$	

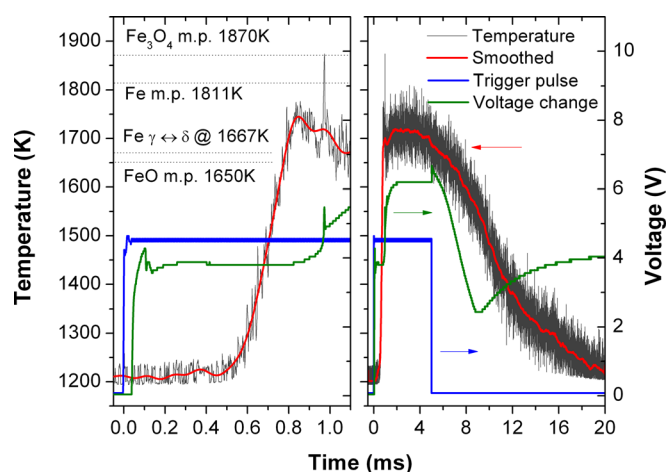


FIG. 9. Time-resolved temperatures of Fe foil in combustion, initiated by electrical pulse heating. The left plots the close-up of the initial 1.1 ms period of the right in the entire time period of the present combustion experiment. The trigger pulse and the voltage change on the sample are shown in blue and green, respectively. The melting points of Fe and related oxides are indicated by dashed horizontal lines. At 0.975 ms when the temperature is beyond the Fe melting point, a sudden voltage jump is observed as a result of sample fracture as in Ti combustion.

Note that the major combustion products of metal monoxide (ZrO , TiO , and FeO) are the most oxygen deficient oxides available at high temperatures near the melts.²³ This result is in sharp contrast to the previous combustion results showing ZrO_2 and TiO_2 to be the major products precipitated out from oxygen saturated (Zr , Ti)-O solutions.^{5,24–26} In the work of Kovalev *et al.*,²⁵ the combustion process was examined in a relatively low time-resolution of about 0.1–1 s, providing substantially longer time for oxygen diffusion and preferentially capturing relatively slow reaction products in the later time of combustion. Molodetsky *et al.*,⁵ on the other hand, found nonstoichiometric oxides in quenched Zr particles in their microprobe chemical analysis of the

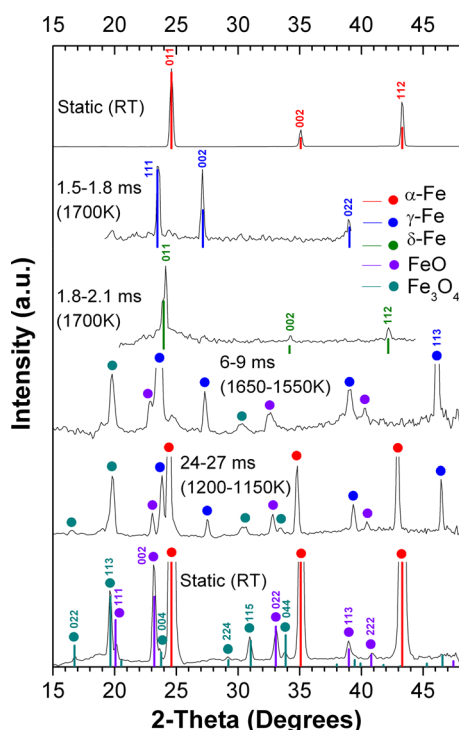


FIG. 10. Time-resolved x-ray diffraction patterns of Fe strip in combustion in air. The simulated diffraction peaks are superimposed as marked by vertical color lines. The indices of each phase are also indicated.

combustion products, but could not resolve the crystal structures. The ability to obtain the structural evidence for the fast combustion products such as ZrO, TiO, and FeO, therefore, signifies the utility of the present fast (μ s) time-resolved powder x-ray diffraction in real-time investigation of rapid combustion reactions.

Moreover, the kinetically (or diffusion) controlled combustion process gives rise to multiple phases that are not present in the equilibrium phase diagrams or under equilibrium conditions. These include metastable phases ZrO and high temperature phases of cubic-ZrO₂ and γ -TiO, quenched

at high cooling rates of 10^4 – 10^5 K/s. Previous research observed metastable ZrO on the surface of ZrC upon oxidation at 1000 °C²⁷ or during the heating of Zr metals in steam with the presence of hydrogen or with oxides of Fe, Co, and Ni.²⁸ The ZrO produced was in a small amount and mixed with other oxides because of its instability. In contrast, ZrO is the dominant oxide in the present final combustion products and is the only crystallized phase from the molten Zr metal at the initial stage of combustion. This indicates that the high temperature, rapid heating and cooling, and limited oxygen in combustion create favorable conditions for the formation of ZrO, which may provide an alternative route for the large scale synthesis.

B. Secondary interfacial reactions between metal monoxides and metals

In parallel to oxygen diffusion continuously occurring from the surface to the center of the metal foils through the already formed oxide layers under the driving force of concentration gradient, the coexistence of multiple phases creates a series of interfacial boundaries and a variety of phase transformation and reaction could occur simultaneously in different regions and interfaces. These secondary reactions are important to the entire combustion process because they would alter the energy flowing pathway and reaction period in the later stage and thus the combustion dynamics and kinetics. At the outer surface layer in contact with the air, monoxides react with oxygen to form the highest stoichiometric metal oxides such as ZrO₂ and TiO₂. However, their contents are relatively small in the final combustion products ($\sim 7\%$, see Tables I).

At the inner interface between monoxides and unreacted metals, their reaction leads to the formation of even lower suboxides such as Zr₃O and Ti₃O/Ti₂O (see Figs. 5 and 8) at temperatures around 600–500 K, estimated based on the exponential extrapolation of the time-resolved temperatures in Figs. 2 and 7. This is then consistent with their presence at the low temperature regime as indicated in the phase

TABLE III. Crystal structures and lattice parameters of Fe and its oxides formed in combustion.

Phase	Content (at. %)	Lattice system	Space group	Lattice parameters (\AA)		PDF#
				This work	Literature	
α -Fe (Static)	87	Cubic	$Im\bar{3}m$	$a = 2.868$ $b = 2.868$ $c = 2.868$	$a = 2.8664$ $b = 2.8664$ $c = 2.8664$	87-0721
γ -Fe (1.5–1.8 ms)	-	Cubic	$Fm\bar{3}m$	$a = 3.679$ $b = 3.679$ $c = 3.679$	$a = 3.671$ $b = 3.671$ $c = 3.671$	
δ -Fe (1.8–2.1 ms)	-	Cubic	$Im\bar{3}m$	$a = 2.934$ $b = 2.934$ $c = 2.934$	$a = 2.933$ $b = 2.933$ $c = 2.933$	
FeO (Final)	10.4	Cubic	$Fm\bar{3}m$	$a = 4.286$ $b = 4.286$ $c = 4.286$	$a = 4.294$ $b = 4.294$ $c = 4.294$	75-1550
Fe ₃ O ₄ (Final)	2.6	Cubic	$Fd\bar{3}m$	$a = 8.391$ $b = 8.391$ $c = 8.391$	$a = 8.393$ $b = 8.393$ $c = 8.393$	
						85-1436

diagrams.^{23,29,30} The stoichiometric composition of Zr_3O and Ti_2O represents the upper solubility limit of oxygen in $\alpha\text{-Zr}$ and $\alpha\text{-Ti}$, respectively.

It is known that oxygen atoms are diffused into the octahedral interstitials of the hexagonally closed-packed $\alpha\text{-Zr}$, $\alpha\text{-Ti}$ layers ($P6_3/mmc$).³¹ High concentration gradients, high oxygen permeability of cubic ($Fm-3m$) ZrO/TiO ,³² and relatively low Zr/Ti-O ionization energies³³ facilitate the oxygen diffusion through already formed solid ZrO/TiO layers, but only slowly over 12 – 36 ms (see Figs. 5 or 8). At the boundary, oxygen atoms of TiO diffuse into every other layers of octahedral interstitials in $\alpha\text{-Ti}$, giving rise to the trigonal structure of Ti_2O ($P-3m1$) with threefold coordinated Ti atoms and sixfold coordinated O atoms. At the farther from the boundary into the sample center, the oxygen content further decreases. As a result, Ti is only coordinated with two O atoms and the resulting compounds are Ti_3O ($P-31c$). Unlike in $\alpha\text{-Ti}$, oxygen atoms are partially filled in every layer of octahedral interstices in $\alpha\text{-Zr}$, resulting in Zr_3O .

In contrast to Zr and Ti, we observed only FeO and Fe_3O_4 — the products stable in iron-rich end of the Fe-O_2 binary phase diagram — without other Fe oxides such as Fe_2O_3 . Because of a small difference in the solidification temperatures (1650 vs 1870 K), Fe_3O_4 precipitates out nearly simultaneously with FeO (see Fig. 10) at relatively high temperatures above 1600 K (see Fig. 9) in relatively early time of combustion. As a result, FeO and Fe_3O_4 form the primary products, but only as the minor (13%) final products together with the major unreacted iron (87%). The absence of the secondary products in the later time, on the other hand, indicates the stronger Fe–O bonds and the smaller oxygen permeability in solids FeO and Fe_3O_4 , than those of ZrO and TiO . Hirano *et al.* also found that the majority of the final oxides was Fe_3O_4 with only trace amount of Fe_2O_3 in their studies on burning iron rods even in the high-pressure oxygen gas environment.³⁴

C. Dynamic thermal expansion of iron

The time-resolved structural data can provide the fundamental thermodynamic information such as the volume expansivity of iron, as shown in Fig. 11. In order to collect sufficient data points for analysis, we employ relatively low current and long heating time in this experiment. The heating rate is measured to be $\sim 1.4 \times 10^5$ K/s, which is an order of magnitude lower than the typical heating rate ($\sim 10^6$ K/s) mentioned during the combustion. There are three polymorphs of Fe at ambient pressure including $\alpha\text{-Fe}$, $\gamma\text{-Fe}$, and $\delta\text{-Fe}$. As calculated from Fig. 11, the volume expansion of iron is measured to be about 3.3% for $\alpha\text{-Fe}$ and 2.2% for $\gamma\text{-Fe}$, which yields the thermal expansion coefficient as defined by $1/V(\Delta V/\Delta T)_p$ of about $3.3 \times 10^{-5}/\text{K}$ for $\alpha\text{-Fe}$ and $6.5 \times 10^{-5}/\text{K}$ for $\gamma\text{-Fe}$. These values compare similarly with those measured under static conditions ($3.5 \times 10^{-5}/\text{K}$ at 293 K and $7.0 \times 10^{-5}/\text{K}$ at 1500 K).³⁵

Because the bcc structure is more open than the fcc (the packing of 68% vs 74%), the specific volume contracts upon the $\alpha \rightarrow \gamma$ transition and increases upon the $\gamma \rightarrow \delta$ transition. These transitions accompany abrupt volume changes of

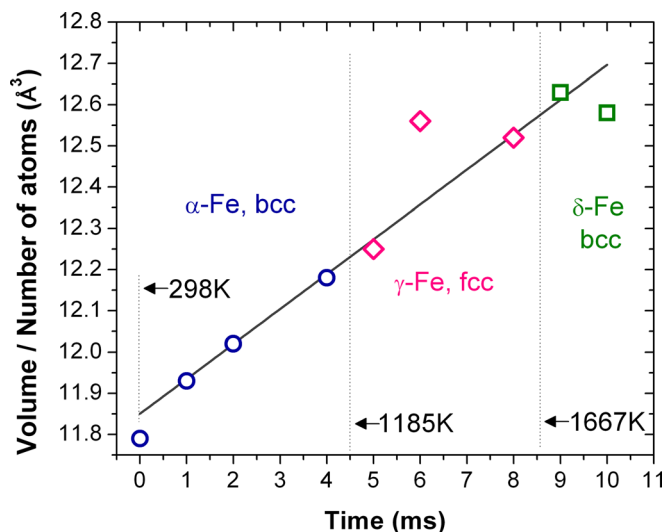


FIG. 11. The specific volume expansion of Fe measured in the heating stage of combustion and plotted as a function of heating time. The transition temperatures are also noted in the figure for the $\alpha\text{-}\gamma$ and $\gamma\text{-}\delta$ phase transitions.

about 1–1.5% under slow heating conditions.³⁶ In this regard, it is interesting to note that the volume discontinuity is not apparent under the present fast heating conditions. The absence of the volume discontinuity may be due to the fast heating rate of $\sim 10^5$ K/s and the relatively slow structural relaxation after the phase transition.

V. CONCLUSION

We have reported the structural and chemical changes associated with metal combustion processes of three transition metal strips (Zr, Ti, and Fe), obtained using time-resolved synchrotron x-ray diffraction and time-resolved optical spectro-pyrometry. The results indicate that the combustion occurs at the heating rates of $\sim 10^6$ K/s to the peak temperatures well beyond the melting temperatures of the metals or their oxides: $T_B(\text{Zr}) = 3200$ K, $T_B(\text{Ti}) = 2600$ K, and $T_B(\text{Fe}) = 1900$ K. After undergoing a series of polymorphic phase transitions, the combustion reactions occur from the molten metals to produce transition metal monoxides (ZrO , TiO , and FeO) in the early stage of combustion, then unusual suboxides (Zr_3O and $\text{Ti}_3\text{O/Ti}_2\text{O}$) in the later stage. The metal dioxides (ZrO_2 and TiO_2) are observed mainly on the surface of the metal strips. These results clearly underscore the oxygen-diffusion limited combustion reactions of metal strips.

The present study highlights that a “simple” process like Zr combustion is not simple at all, but involves rather complex structural and chemical changes: $\alpha\text{-Zr} \rightarrow \beta\text{-Zr} \rightarrow \text{liquid-Zr} \rightarrow \text{fcc-ZrO} \rightarrow \text{trigonal-Zr}_3\text{O} + \text{cubic-ZrO}_2$. Some of these processes occur exothermically, fueling other secondary reactions and altering the dynamics of the combustion reactions. These processes are barely the same as $\text{Zr} + \text{O}_2 \rightarrow \text{ZrO}_2$, what has been assumed in many commonly used integrated chemical models and hydro-codes. Therefore, obtaining the accurate information regarding these dynamic structural and chemical changes is the priority for going beyond an energetic use of metal combustions, to

developing a predictive capability and, ultimately, controlling the reaction mechanisms, dynamics, and kinetics of metal combustion processes.

ACKNOWLEDGMENTS

The x-ray work was done using the HPCAT beamline (16IDD) of the APS. We appreciate Dr. P. Chow and Dr. Y. Xiao for their assistance at the beamline. HPCAT is supported by CIW, CDAC, UNLV and LLNL through funding from DOE-NNSA, DOE-BES and NSF. APS is supported by DOE-BES, under Contract No. DE-AC02-06CH11357. The present study has been supported by the U.S. DHS under Award Number 2008-ST-061-ED0001 and the NSF-DMR (Grant No. 0854618). The views and conclusions contained in this document are those of the authors and should not be interpreted as necessarily representing the official policies, either expressed or implied, of the U.S. Department of Homeland Security.

- ¹E. L. Dreizin, *Combust. Explos. Shock Waves* **39**, 681 (2003).
- ²M. A. Trunov, M. Schoenitz and E. L. Dreizin, *Propellants, Explos., Pyrotech.* **30**, 36 (2005).
- ³M. W. Beckstead, B. R. Newbold, C. Waroquet, A Summary of Aluminum Combustion, JANNAF 37th Combustion Subcommittee Meeting, Vol. 1, CPIA Publ. 701, 485 (2000).
- ⁴H. Wei and C. S. Yoo, *J. Appl. Phys.* **111**, 023506 (2012).
- ⁵I. E. Molodetsky, E. L. Dreizin, and C. K. Law, *Sym. (Int.) Combust., [Proc.]* **26**, 1919 (1996).
- ⁶E. L. Dreizin, *Combust. Flame* **105**, 541 (1996).
- ⁷M. E. Reiss, C. M. Esber, D. Van Heerden, A. J. Gavens, M. E. Williams, and T. P. Weihs, *Mater. Sci. Eng., A* **261**, 217 (1999).
- ⁸V. I. Levitas, B. W. Asay, S. F. Son, and M. Pantoya, *Appl. Phys. Lett.* **89**, 071909 (2006).
- ⁹B. S. Bockmon, M. L. Pantoya, S. F. Son, B. W. Asay, and J. T. Mang, *J. Appl. Phys.* **98**, 064903 (2005).
- ¹⁰K. J. Blobaum, D. Van Heerden, A. J. Gavens, and T. P. Weihs, *Acta Mater.* **51**, 3871 (2003).
- ¹¹K. Fadenberger, I. E. Gunduz, C. Tsotsos, M. Kokonou, S. Gravani, S. Brandstetter, A. Bergamaschi, B. Schmitt, P. H. Mayrhofer, C. C. Doumanidis, and C. Rebholz, *Appl. Phys. Lett.* **97**, 144101 (2010).
- ¹²E. G. Gillan and R. B. Kaner, *J. Mater. Chem.* **11**, 1951 (2001).
- ¹³R. G. Blair, A. Anderson, and R. B. Kaner, *Chem. Mater.* **17**, 2155 (2005).
- ¹⁴C. S. Yoo, H. Wei, J.-Y. Chen, G. Shen, P. Chow, and Y. Xiao, *Rev. Sci. Instrum.* **82**, 113901 (2011).
- ¹⁵S. Goroshin, D. L. Frost, J. Levine, A. Yoshinaka, and F. Zhang, *Propellants, Explos., Pyrotech.* **31**, 169 (2006).
- ¹⁶D. Partouche-Sebban, D. B. Holtkamp, J. L. Pelissier, J. Taboury, and A. Rouyer, *Shock Waves* **11**, 385 (2002).
- ¹⁷C.-S. Yoo, H. Wei, R. Dias, G. Shen, J. Smith, J.-Y. Chen and W. Evans, Time-Resolved Synchrotron X-ray Diffraction on Pulse Laser Heated Iron in Diamond Anvil Cell J. Phys. Conf. Ser. (in press).
- ¹⁸L. S. Nelson, *Sym. (Int.) Combust., [Proc.]* **11**, 409 (1967).
- ¹⁹L. S. Nelson, D. E. Rosner, S. C. Kurzius, and H. S. Levine, *Sym. (Int.) Combust., [Proc.]* **12**, 59 (1969).
- ²⁰C. J. Gilbert, J. W. Ager, V. Schroeder, R. O. Ritchie, J. P. Lloyd, and J. R. Graham, *Appl. Phys. Lett.* **74**, 3809 (1999).
- ²¹European Synchrotron Research Facility, www.esrf.eu/computing/scientific/fit2d/.
- ²²W. M. Haynes, *CRC Handbook of Chemistry and Physics*, 92nd ed. (CRC Press, 2011).
- ²³ASM Alloy Phase Diagrams Center, Diagram No. **103569**, 101191, **901814**, 2002001, 101128.
- ²⁴I. E. Molodetsky, E. P. Vicenzi, E. L. Dreizin, and C. K. Law, *Combust. Flame* **112**, 522 (1998).
- ²⁵D. Kovalev, V. Shkuro, and V. Ponomarev, *Int. J. Self-Propag. High-Temp. Synth.* **16**, 169 (2007).
- ²⁶I. O. Khomenko, A. S. Mukasyan, V. I. Ponomarev, I. P. Borovinskaya, and A. G. Merzhanov, *Combust. Flame* **92**, 201 (1993).
- ²⁷H. Kitaoka, K. Ozawa, K. Edamoto, and S. Otani, *Solid State Commun.* **118**, 23 (2001).
- ²⁸N. Schönberg, *Acta Chem. Scand.* **8**, 1460 (1954).
- ²⁹T. Arai and M. Hirabayashi, *J. Less-Common Met.* **44**, 291 (1976).
- ³⁰R. Arroyave, L. Kaufman, and T. W. Eagar, *CALPHAD: Comput. Coupling Phase Diagrams Thermochem.* **26**, 95 (2002).
- ³¹B. Holmberg, *Acta Chem. Scand.* **16**, 1245 (1962).
- ³²G. Knöner, K. Reimann, R. Röwer, U. Södervall, and H.-E. Schaefer, *Proc. Nat. Acad. Sci.* **100**, 3870 (2003); also see, U. Brossman, G. Knöner, H.-E. Scharfer, and R. Würschum, *Rev. Adv. Mater. Sci.* **6**, 7 (2004).
- ³³A. A. Safono, A. A. Bagatur'yants, and A. A. Korkin, *Micro. Eng.* **69**, 629 (2003).
- ³⁴T. Hirano, Y. Sato, K. Sato, and J. Sato, *Oxid. Commun.* **6**, 113 (1984).
- ³⁵Kaye & Laby Tables of Physical & Chemical Constants, National Physical Laboratory, www.kayelaby.npl.co.uk.
- ³⁶H. Mearthur and D. Spalding, *Engineering Materials Science: Properties, Uses, Degradation, Remediation* (Horwood Publishing, Chichester, UK, 2004).
- ³⁷R. W. G. Wyckoff, *Crystal Structures* (Interscience, New York, 1963).
- ³⁸Z. S. Basinski, W. Hume-Rothery, and A. L. Sutton, *Proc. R. Soc. London, Ser. A* **229**, 459 (1955).